Supplementary information for *"Brain organization into resting state networks emerges at criticality on a model of the human connectome"*

Haimovici et al.

FMRI DATA ACQUISITION AND PREPROCESSING

The human brain data discussed in the comparison with the model is taken from previous publications [3, 8]. Data was obtained, after informed consent, from ten right-handed healthy volunteers (9 female, 1 male; mean age=49, S.D.=12), during 10 minutes, requested to keep their eyes closed and to avoid falling asleep. The study was approved by the Clinical Research Ethics Committee of the University of the Balearic Islands (Palma de Mallorca, Spain). fMRI data acquisition was performed with a GE Medical Systems Signa HDx 3 Tesla scanner using echo-planar sequences, 240 volumes were acquired with a TR of 2500 ms, TE of 35 ms, and 90 deg flip angle. Thirty-six slices of 64x64 dimensions were obtained with a field of view of 200 mm and slice thickness of 3 mm. Structural images consisted of a T1-weighted scans of 176x512x512 voxels, with a TR of 7176 ms, TE of 3150 ms, flip angle of 12 deg, FOV 240 mm and slice thickness of 1 mm. Preprocessing of BOLD signal was performed using FMRIB Expert Analysis Tool (http://www.fmrib.ox.ac.uk/fsl), including motion correction using MCFLIRT, slice-timing correction using Fourier-space time-series phase-shifting, non-brain removal using BET and spatial smoothing using a Gaussian kernel of full-width-half-maximum 5 mm. Brain images were normalized to standard space with FLIRT using the MNI 152 template and resampled to 4 mm × 4 mm × 4 mm resolution. Resting functional data was filtered with a zero lag finite impulse response band pass filter (0.01-0.1 Hz).

MODEL: FURTHER DETAILS OF THE NUMERICAL SIMULATIONS

Cluster's definition (Fig. 1)

Clusters are groups of nearest neighbor nodes simultaneously activated. Taken into account that the grain of the parcellation used by Hagmann et al [4] two nodes were considered as first neighbors if the euclidean distance between them was smaller than 2.5 cm. To identify the phase transition, at each time step the size of the giant cluster (S_1) as well as of the second largest cluster (S_2) were computed.

Modeling time series for comparison with fMRI data

For the model results described in Figures 2 and 3, the time series of each node was binarized by assigning state $E = 1$ and the remaining states into 0s. To mimic the coupling between neural and metabolic activity measured in the fMRI experiments the time series were convolved with a standard hemodynamic response function [5] (HRF). The HRF was generated with SPM8 using standard parameters and a sampling rate of 1 s. The signals were then filtered with a zero lag finite impulse response band pass filter (0.01 - 0.1 Hz) as routinely done with the experimental human brain fMRI data. For the fMRI data used in these figures, 998 time series were extracted using the coordinates given by Hagmann et al. [4] as the center of the ROI's and averaging over its nearest neighbors.

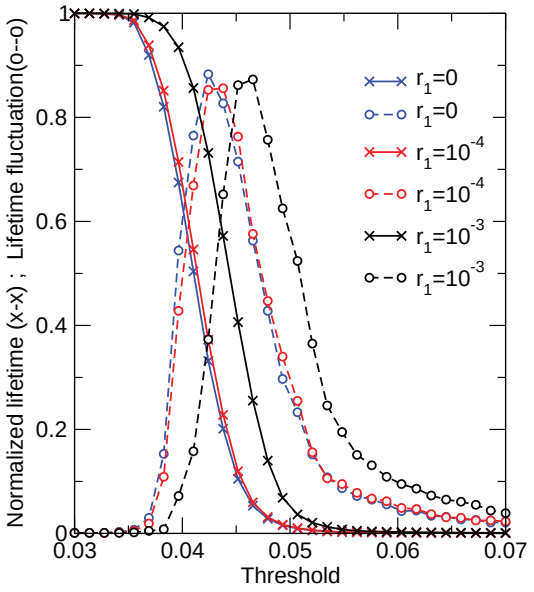


FIG. 1. Normalized lifetimes (full lines) and their dispersion (dashed lines) for three r_1 values as a function of T.

MODEL: CHARACTERIZATION OF THE PHASE TRANSITION IN TERMS OF ACTIVITY LIFETIME

As an additional way to determine the critical point, we computed the activity lifetimes in the model as a function of T. The lifetime is the time elapsed until activity

dies out in the network starting from an initial configuration of excited nodes. This was studied before in this model (see for instance [2], [9], and also [1] in the context of psychophysics). In Fig. S1 we show the (normalized) lifetime and dispersion in the lifetime distributions as a function of T. For an spontaneous excitation rate of $r = 0.001$, the transition occurs between $T = 0.045$ and $T = 0.05$, close to the transition detected by looking at the second largest cluster size (i.e., Figure 1 in the paper). The normalization was done over the longest time of the simulations (10^4 steps). Because of this normalization, variance was not used to compute lifetime variability, instead the number of different lifetime's duration was computed. Notice that, as expected the dispersion of lifetime peaks near the transition.

CHARACTERIZATION OF THE PHASE TRANSITION IN TERMS OF DISTRIBUTION OF CLUSTER SIZES

Another generic feature of phase transition is the scale invariance exhibited by the sizes of clusters of activity. This is only seen near the critical point, otherwise as the system is moved away from criticality this scale invariance disappears and characteristic scales show up. Calculations in the model (see Fig. S2) show that the distribution of cluster sizes obtained only at T_c (red circles) matches the scale invariant distribution computed from the fMRI data (dotted line and crosses).

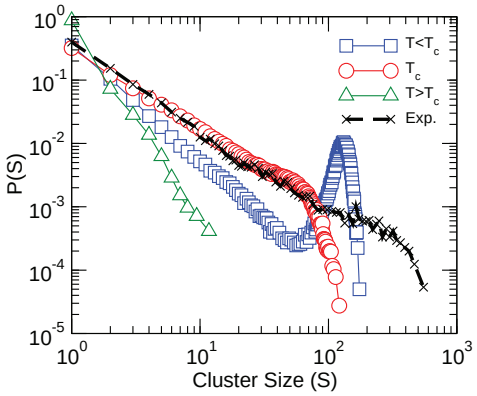


FIG. 2. The distribution of clusters sizes at the critical (T_c) corresponds to what is observed experimentally. The only difference is in the cut off of the power law decay, given by the coarser resolution of the model. In the subcritical regime ($T < T_c$) the distribution shows the presence of a giant cluster, and the supercritical regime (($T > T_c$) shows only a few clusters comprised by a few nodes.

FURTHER DETAILS ON THE COMPUTATION OF THE CORRELATION FUNCTION AND CORRELATION LENGTH

We start subtracting from the nodes in each cluster the mean cluster activity:

$$\tilde{B}(x_i,t) = B(x_i,t) - \frac{1}{N_H}\sum_{i=1}^{N_H} B(x_i,t) \qquad (1)$$

where B is either the BOLD time series in the case of human data or the time series of the model of node i, with position x_i inside the cluster H of size N_H. Next, we computed the average correlation function of the signal fluctuations between all pairs of regions in each cluster which are separated by a distance r:

$$< C_H(r) > = \langle \frac{< (\tilde{B}_{x_i} - \bar{\tilde{B}}_{x_i})(\tilde{B}_{x_j} - \bar{\tilde{B}}_{x_j}) >_t}{\sigma_{\tilde{B}_{x_i}} \sigma_{\tilde{B}_{x_j}}} \rangle_{i,j} \qquad (2)$$

$$\bar{\tilde{B}}_{x_i} = \frac{1}{T_s}\sum_{t=1}^{T_s} \tilde{B}(x_i,t)$$

$$\sigma^2_{\tilde{B}_{x_i}} = \frac{1}{T_s}\sum_{t=1}^{T_s} (\tilde{B}(x_i,t) - \bar{\tilde{B}}_{x_i})^2$$

where T_s is the length of the time series, $<>_t$ stands for the average over time and $<>_{i,j}$ over all pairs of regions i and j that belong to the cluster H and are separated by a distance r.

Power law decay of $C(r)$

The decay of correlation as a function of distance ($C(r)$) can be described for all regimes by the following expression [7],

$$C(r) = \frac{1}{r^{d-2+\eta}} exp\left(-\frac{r}{\xi}\right) \qquad (3)$$

where d is the system dimension, η a critical exponent and ξ is the correlation length. According to this expression, for finite ξ, $C(r)$ decays exponentially with a decay constant of $1/\xi$. At the critical point, ξ diverges as $\xi \sim |T - T_c|^{-\nu}$. The exponential contribution to Eq. 1 is suppressed if ξ diverges, turning into a power law decay with exponent $d - 2 + \eta$. We fitted the decay of $C(r)$ with a straight line in logarithmic coordinates and obtained the average goodness of fit across all cluster sizes ($< R^2 >$) as a function of T. Results are shown in Fig. S3. As expected by the divergence of ξ, the best fit is obtained around the critical point.

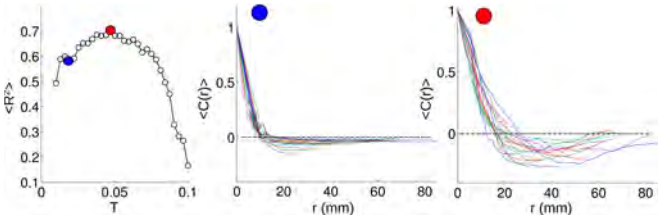


FIG. 3. Left: $< R^2 >$ as a function of T. Middle: $C(r)$ for all cluster sizes at the super-critical regime. Right: $C(r)$ for all cluster sizes at the critical regime.

Scaling relations without discarding nodes

Figs. 2 and 3 of the manuscript correspond to numerical simulations using only those nodes with a location no farther than 1 cm away from any RSN. This criterion, which is a reasonable one for comparing with empirical data, nevertheless excludes $\approx 19\%$ of the 998 nodes. To verify that the results still hold when including all the nodes, we repeated the computations assigning each node to the closest RSN (without restrictions on the distance). Results are shown in Figs. S4 and S6. The simple inspection of these two figures, reveals that the main results of the paper still hold, including or excluding these nodes.

Fluctuations of the short term $< C >$ time series for all clusters

In Fig. 2A of the paper we provide examples of $< C >$ time series for one subject and three representative cluster sizes. To demonstrate that the examples selected for the paper are representative, in Fig. S5 we show the $< C >$ time series for all subjects/trials (concatenated one after the other only for presentation purposes), for all cluster sizes and dynamical regimes. Please notice that time series for different subjects/model trials are separated by red vertical lines.

FURTHER DETAILS OF THE COMPARISON BETWEEN FMRI RSN AND MODEL

Random growth algorithm for the 998 seeds

To identify the model RSN in the same way done with human brain data we need to compute ICA from data constructed from the model at different dynamical regimes.

To compare with human RSN data (Figure 4), we need to resample the model expanding the 998 nodes to the entire brain and to assign a time series to each voxel. We start with the coordinates of 998 cortical and sub-cortical regions from Hagmann et al [4], whose anatomical connectivity is used to define the underlying connectivity of our model.

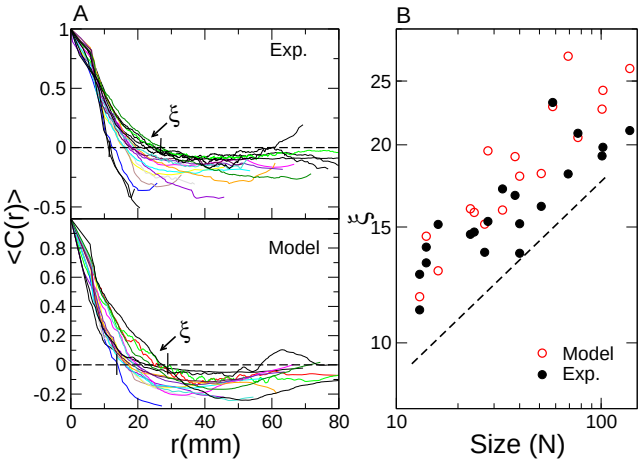


FIG. 4. The correlation length ξ of the activity in the model near T_c increases with the cluster size (N), as reported for human brain data [3]. Panel A shows the correlation function $C(r)$ computed from human data (Exp.) and from the model at T_c (colored lines are used for the different clusters). The correlation length ξ is the distance r where $C(r) = 0$, seen here to span a range (denoted with the arrows). Panel B shows the ξ values for the functions plotted on panel A, demonstrating that $\xi \sim N^{1/3}$ (dashed line), both in the experiment and model data. These results were computed assigning each of the 998 nodes to the closest RSN (i.e., without discarding any node).

According with Hagmann et al. [4] the x, y, z coordinates provided for each node represent the center of an area of approx. 1.5 cm^2 of flattened cortex. Thus, in order to obtain a complete covering of the human gray matter, each of the 998 nodes has to be uniformly extended into patches centered at each one of the 998 seeds. For this purpose, we iteratively grow each patch (starting from a single voxel at each seed coordinate) by adding neighboring voxels to it if they are included in the gray matter and are not already part of another patch, until no more voxels can be added. The resulting parcellation is shown in Fig. S 7. We computed the area of cortex surface covered by each patch, resulting on an average of 224 ± 150 mm^2.

After the parcellation was obtained, the time series of each seed was assigned to all the voxels in the corresponding patch and independent gaussian noise of relatively small variance was added to all voxels. This 4D image was then used to obtain the model ICA using MELODIC FSL, as explained below.

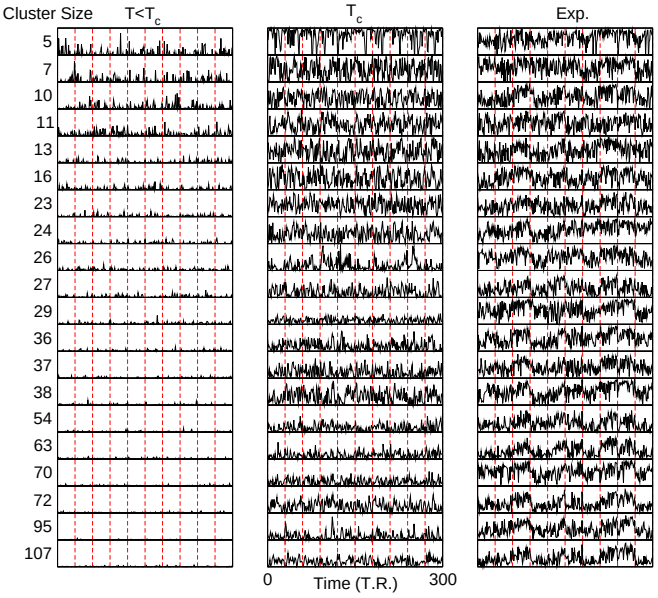


FIG. 5. $< C >$ time series for all clusters sizes, subjects, and trials (separated by red vertical dashed lines). Notice that for all the realizations with $T < T_c$ (left column) the variance of the short term correlation decreases rapidly as cluster size increases. In contrast the experimental results from all subjects shows a constant amplitude, which is best replicated by the simulations with $T = T_c$ which show only a small decline in the variance.

Independent Component Analysis

The spatial locations of the RSN reported in Figure 4 were identified using the Probabilistic Independent Component Analysis as implemented in MELODIC (Multivariate Exploratory Linear Decomposition into Independent Components) Version 3.10, which is part of the FSL package (FMRIB's Software Library, www.fmrib.ox.ac.uk/fsl).

The following data pre-processing was applied to the input data: masking of non-brain voxels; voxel-wise demeaning of the data; normalization of the voxel-wise variance. Pre-processed data were whitened and projected into a 8-dimensional subspace using Principal Component Analysis. The whitened observations were decomposed into sets of vectors which describe signal variation across the temporal domain (time-courses) and across the spatial domain (maps) by optimizing for non-Gaussian spatial source distributions using a fixed-point iteration technique. Estimated component maps were divided by the standard deviation of the residual noise and thresholded by fitting a mixture model to the histogram of intensity values.

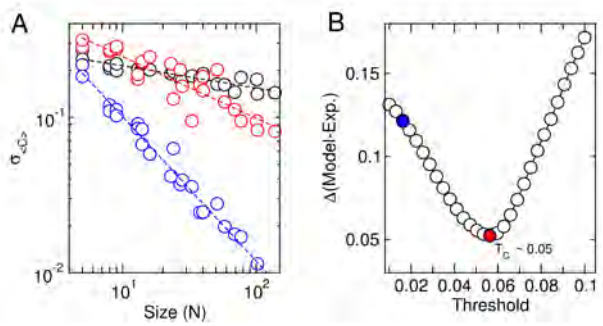


FIG. 6. The short-term correlation $< C >$ in the model at T_c exhibits transient fluctuations at all cluster sizes as seen in human brain data [3]. Panel A shows that the variance of the fluctuations in $< C >$ remains approximately constant only for the human brain data (empty black circles) and for the model at T_c (filled red circles). For $T < T_c$ (filled blue circles) the variance decreases faster with N. Panel B shows a plot of the distance between the scaling of the fluctuations of the human fMRI data and those from the model for a wide range of T. Notice that the best agreement occurs for T_c. These results were computed assigning each of the 998 nodes to the closest RSN (i.e., without discarding any node).

Computation of the similarity between human RSN and model independent components

The $< r >$ data plotted in Fig. 4 of the paper (inset in each of the right panels) represents the mean maximal spatial correlation between the model independent components (IC) and each of the RSN, across 100 runs of the model. To compute the mean maximal spatial correlation, both 3D maps (human brain RSN and model IC) were binarized (thresholding all non-zero voxels to 1) and then Pearson's correlation coefficient between both images was obtained. This correlation was performed between each model IC and all RSN, selecting the RSN with highest correlation and averaging the corresponding correlations across trials (for each value of T). The z values plotted in the brain maps of Fig. 4 (for the human RSN and model IC) represent the statistical confidence that each voxel is included in the corresponding IC. For each choice of T, these statistical confidence maps were averaged across all 100 trials. In addition a null hypothesis was computed, i.e., the T-statistic $t(W - W_{rand})$ for the difference in the correlations obtained using the real connectome and a randomized version of it. This randomization is commented in the next paragraph.

Computation of the independent components from a randomized connectome

We have constructed a null model by simulating activity time series extracted from a model with a randomized



FIG. 7. Parcellation of the human gray matter into 998 patches. Each region is centered in the 998 seed's coordinates reported in [4].

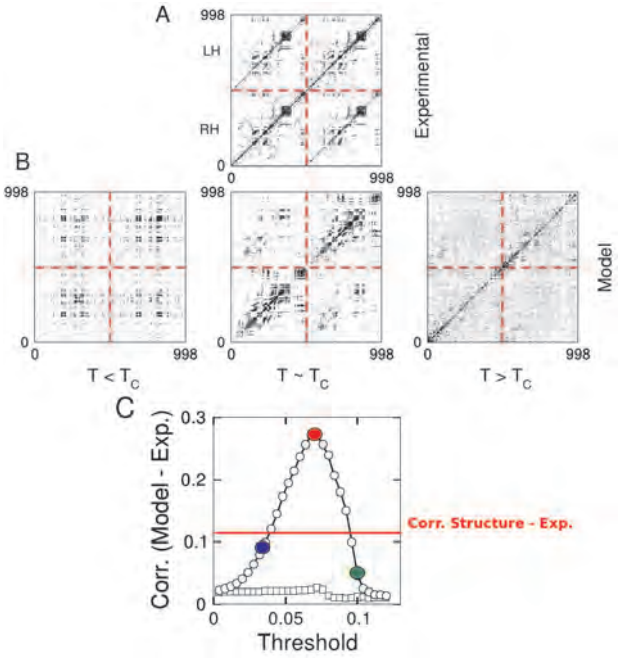


FIG. 8. Panel A: Empirical functional connectivity matrix obtained from the human fMRI data, averaged across all subjects. Panel B: Simulated functional connectivity matrix at three different regimes of the model. Panel C: Correlation between empirical and simulated connectivity matrices (empty circles) and the same computation repeated using a randomized version of the connectome (empty squares). Notice that the best agreement between model and human data is obtained near criticality. For comparison, the linear correlation between the human fMRI functional connectivity matrix (i.e., plotted in Panel A) and the structural connectivity (i.e., Fig. 1 of the paper) matrices is depicted by the horizontal red line ($r \approx 0.11$).

structural connectivity. Specifically, we performed a degree preserving randomization of the human connectome network, implemented by using the Brain Connectivity Toolbox (https://sites.google.com/site/bctnet/) [6], collecting 100 different realizations of this randomized connectome. We then simulated the dynamics using this randomized connectome, in the same way as it was done for the original connectome. We then mapped the time series into the corresponding anatomical locations and applied ICA to this data, as done for the time series obtained with the real connectome. We reported the correlation between the IC obtained this way and the RSN obtained from the fMRI data, as well as the T-statistic for the difference in the correlation distributions obtained using both connectomes (real and randomized).

COMPARISON AT THE LEVEL OF FUNCTIONAL AND STRUCTURAL CONNECTIVITY MATRICES

We computed the correlation matrix both for the simulated time series (as a function of threshold T) and experimental fMRI data (averaged across all subjects). This matrix has in its i, j entry the correlation between the time series of the $i-th$ and $j-th$ regions. We then computed the correlation between the simulated and experimental matrices as a function of T, results are shown in Fig. S8. In Panel A we show the average functional connectivity (or correlation) matrix averaged across all subjects. In Panel B we illustrate the simulated correlation matrices for the three different dynamical regimes (supercritical, critical and subcritical, respectively). In Panel C we plot the correlation between the two as a function of T, using both the real connectome (empty circles) and the randomized version (empty squares). It is clear that the agreement between structural and functional connectivity peaks around T_c. Furthermore, correlation between the empirical functional connectivity matrix and the structural connectivity matrix was lower ($\approx$ 0.11, marked with an horizontal red line in Panel C). This strongly suggests that functional connectivity in the simulated activity time courses predicts the empirical functional connectivity better than expected from the connectome alone (but only around T_c).

[1] O. Kinouchi & M. Copelli. *Nature Physics* **2**, 348 - 351 (2006).

[2] M. Copelli & P. R. A. Campos. *Eur. Phys. J.* **56**,273-278 (2007).

[3] D. Fraiman and D.R. Chialvo, *Front. Physiol.* **3**, 307 (2012).

[4] P. Hagmann, L. Cammoun, X. Gigandet, R. Meuli, C.J. Honey, V.J. Wedeen, O. Sporns, *PLoS Biol.* **6**, e159 (2008).

[5] K.J. Friston, C.D. Frith, R. Turner, R.S.J. Frackowiak, *Neuroimage* **2**, 157 (1995).

[6] M. Rubinov & O. Sporns, *Neuroimage* **52**, 1059-1069 (2010).

[7] A. Lesne & M. Laguës. Scale invariance: From phase transitions to turbulence (Springer, Berlin, 2012).

[8] E. Tagliazucchi, P. Balenzuela, D. Fraiman, D.R. Chialvo, *Front. Physiol.* **3**, 15 (2012).

[9] A. Wu, X. Xu, Y. Wang, *Phys. Rev. E* **75**, 032901(2007).